An Electrically Conductive $CuMn_2O_4$ Ultrananospinel Cathode for Room-Temperature Magnesium Rechargeable Batteries

Reona Iimura,[a] Hiroto Watanabe,[b] Toshihiko Mandai,[c] Itaru Honma,[a] Hiroaki Imai,[b] and Hiroaki Kobayashi*[a,d]

[a]Institute of Multidisciplinary Research for Advanced Materials, Tohoku University, Sendai 980-8577, Japan.

[b]Department of Applied Chemistry, Faculty of Science and Technology, Keio University, Yokohama 223-8522, Japan.

[c]Center for Green Research on Energy and Environmental Materials, National Institute for Materials Science (NIMS), Tsukuba 305-0044, Japan.

[d]Department of Chemistry, Faculty of Science, Hokkaido University, Sapporo 060-0810, Japan.

E-mail: h.kobayashi@sci.hokudai.ac.jp

ABSTRACT: Magnesium rechargeable batteries are potential successors to lithium-ion batteries owing to their low cost, superior safety, and high volumetric energy density. However, the development of high-energy and high-rate cathode materials remains challenging. Oxide-type cathodes, specifically spinels, have become a focus of attention due to their higher voltage operation capacity. Nevertheless, previous studies have predominantly centered on high-temperature operations on account of the sluggish diffusion of Mg ions in solids and low electrical conductivity. In this study, an electrically conductive $CuMn_2O_4$ ultrasmall (< 5 nm) spinel is fabricated using an alcohol reduction process. This 'ultrananospinel' shows a semi-reversible phase transition along with Mg insertion/extraction and a dual-redox system involving copper and manganese ions, exhibiting the high voltage operation (>1.5 V) with a theoretical discharge capacity of 225 mAh g^{-1}, and high-rate capability compared with other oxide-type cathodes.
KEYWORDS: *spinel; nanoparticles; electrical conductivity; cathode; magnesium rechargeable battery*

INTRODUCTION

The widely used lithium-ion batteries (LIBs) have a theoretical energy density limit.[1] As we advance toward an increasingly electrified society, a significant enhancement in battery performance is crucial for the successful adoption of electric vehicles and smart grids. Faced with current global economic instability, there is an increasing demand for batteries that utilize inexpensive metals and are less susceptible to price fluctuations. Magnesium rechargeable batteries (MRBs) are emerging as promising solutions to satisfy these increasingly stringent demands. They are projected to become the next-generation batteries, distinguished by their low cost, superior safety, and high volumetric energy density.[2-5]

A primary challenge for the successful implementation of MRBs is the development of high-energy cathode materials. In 2000, Aurbach *et al*. reported the Chevrel-type Mo_6S_8 as the first prototype battery capable of room-temperature operation.[6] This pioneering work using sulfide cathode materials instigated the proposal of other promising cathode materials, including CuS[7-9] and VS_4.[10-11] Although these sulfide-based cathodes demonstrate impressive cyclability in full-cell batteries, they operate at low voltages (less than 1.2 V), which could potentially result in decreased energy density, thereby inhibiting their commercial viability. In recent years, transition-metal oxide-type cathodes have attracted significant interest owing to their higher operational voltages.[12-13] Among the various oxide-type cathodes, including spinel-type,[14-16] layered-type,[17] and tunnel-type,[18] spinel-type oxides such as $MgTM_2O_4$ (TM: transition metal; Cr, Mn, Fe, Co, etc.) have exhibited the ability to either extract or accommodate significant amounts of Mg ions via a spinel-to-spinel transition or a spinel-to-rock salt transition. An example of a spinel-to-spinel transition is the $MgCrMnO_4$ cathode material.[19-20] The spinel lattice structure was maintained during the removal of Mg^{2+} without any phase transformations in the intermediate temperature range. In comparison, $MgTM_2O_4$ can accommodate Mg ions at high voltage levels (> 2.3 V), and achieve reversible phase transitions at 423 K.[14]

While much of the research in this field has been focused on an elevated-temperature operation to address the slow diffusion of Mg ions in solid-state conditions, we have demonstrated the nanoparticulation of cathode materials for room-temperature MRB operation, as reducing the diffusion length of Mg ion.[21-23] As previously reported, we successfully synthesized ultrasmall and ultraporous $MgMn_2O_4$ (ultrananospinel; < 2.5 nm, 506 m^2 g^{-1}), and the post-annealed material exhibited a theoretical discharge capacity of 270 mAh g^{-1}.[24] Despite its superior cathode characteristics in the room-temperature MRB full-cell test, its current density was only 10 mA g^{-1}; it is essential to improve rate capability for practical use. Very recently, Ingram *et al*. reported that the Mg-based oxide cathodes have much lower electrical conductivity (ca. 10^{-12} S cm^{-1} in $MgCr_2O_4$) compared with LIB cathodes,[25] hence electrically conductive oxides, having more strongly correlated electron system, should be utilized. In addition, more specifically, the rock salt – fully discharged phase – is electrochemically irreversible; the Mg-ion diffusion coefficient of rock salt is 10^{25} times higher than that of spinel phase.[24] Therefore, coherent redox reactions operated at room temperature is challenging. Given these circumstances, development of electrically conductive, and crystallographically and electrochemically stable nanospinels must be required for advancing MRB cathode technology.

In this study, we focus on replacing the Mg element in $MgMn_2O_4$ 'ultrananospinel' with transition metals, such as Cu and Co, having a correlated electron system that can exhibit higher electric conductivity compared with Mg. We fabricated and investigated various 'ultrananospinels', Mg-Mn, Co-Mn, and Cu-Mn spinels composed of approximately 5 nm-sized primary particles, for room temperature MRB cathodes. The Cu-Mn ultrananospinel ($CuMn_2O_4$) exhibited a significantly higher electrical conductivity, demonstrating the high energy density and high rate capability, achieving a discharge capacity twice that of the other spinels in a room-temperature MRB full-cell operation.

RESULTS AND DISCUSSION

Ultrasmall A-Mn spinels, referred to as MgMO, CoMO, and CuMO, with "A" being Mg, Co, and Cu, respectively, were developed using a modified alcohol reduction process,[21, 26] as illustrated in Figure 1. Initially, Mn^{7+} from *n*-Bu_4NMnO_4 was reduced by methanol and promptly reacted with other metals to form Mn binary oxides. With the addition of H_2O, a dark brown precipitate was formed, and after subsequent washing and drying, Mn binary spinels were successfully obtained.

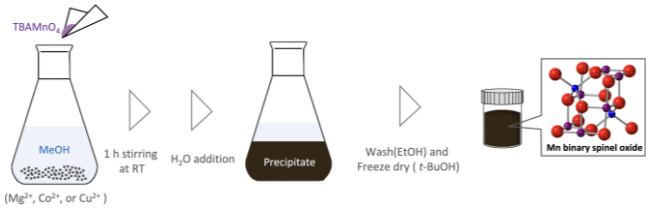

Figure 1. Schematic illustration of synthesizing AMO (A=Mg, Co, and Cu).

The synthesized Mn binary oxides presented markedly broad XRD patterns, suggesting the formation of nanocrystals (Figure 2a). As stated in our previous reports, these synthesized Mn-binary oxides, including the newly synthesized ultrasmall Cu-Mn oxides, were attributed to a single phase of cubic spinel with the *Fd*–3m space group by Rietveld analysis.[27] As illustrated in Figure 2b and S1b, the diffraction patterns of CuMO and MgMO correspond to the XRD results, indicating the formation of spinels. The selected area electron diffraction (SAED) analysis of CoMO shown in Figure S1a not only reveals the diffraction rings correlating to the obtained XRD pattern but also reveals a diffraction ring corresponding to 111 diffraction, indicating the formation of Co-Mn spinel, note that the 111 diffraction at 18° of CoMO is too faint and broad to detect. As listed in Table S1, the chemical compositions of the obtained samples were determined using scanning electron microscopy-energy dispersive X-ray analysis (SEM-EDX). The results indicate that MgMO and CuMO exhibit an atomic ratio of Mg (or Cu) to Mn of approximately 1/2, which is also supported by the ICP-AES result (Cu/Mn =0.48), suggesting the formation of $MgMn_2O_4$ and $CuMn_2O_4$ spinels. In contrast, CoMO shows a high atomic ratio of Co to Mn (Co/Mn = 0.69), which differs from a previous report.[26] This discrepancy may be attributed to the use of different solvents because the choice of solvent can affect the behavior of the Mn redox reaction with other cations. In this study, we utilized MeOH, which has a lower oxidation potential than the previously used *i*-PrOH.[28] Figure 2c shows SEM images of CuMO. The images reveal that CuMO is characterized by a porous structure formed by secondary particles ranging from tens to hundreds of nanometers in size. This finding suggests effective suppression of particle aggregation. Indeed, according to BET analysis, the specific surface area of CuMO is 295 $m^2\ g^{-1}$, which is comparable to CoMO (284 $m^2\ g^{-1}$). MgMO has a larger specific surface area (436 $m^2\ g^{-1}$), which stems from its higher porous structure.

Figure 2d and Figure S2 display high-resolution transmission electron microscopy (HR-TEM) images of each sample. Approximately 5 nm-sized primary particles were aggregated to form secondary particles. Figure 2e illustrates the Fourier-transform infrared spectroscopy (FT-IR) spectra of the spinels. As shown in the figure, the signals at 600 cm^{-1}, 1400 cm^{-1}, 1600 cm^{-1}, and 3200 cm^{-1} are attributed to the Mn-O-Mn lattice mode, OH bending, Mn-OH bending, and OH stretching, respectively. Of these signals, only the Mn-OH bending signal should originate from the surface OH groups, as the other OH signals are likely to be influenced by absorbed H_2O. To further examine the relative quantities of surface OH, we summarize the peak area ratio of Mn-OH to Mn-O-Mn in Figure 2f. Thus, MgMO possesses the highest surface-OH quantity, whereas CuMO has the lowest. A potential explanation for this variation could be the difference in electronegativity: Mg-O (2.13), Co-O (1.56), and Cu-O (1.54).[29] There appears to be a positive correlation between these values and the amount of surface OH.

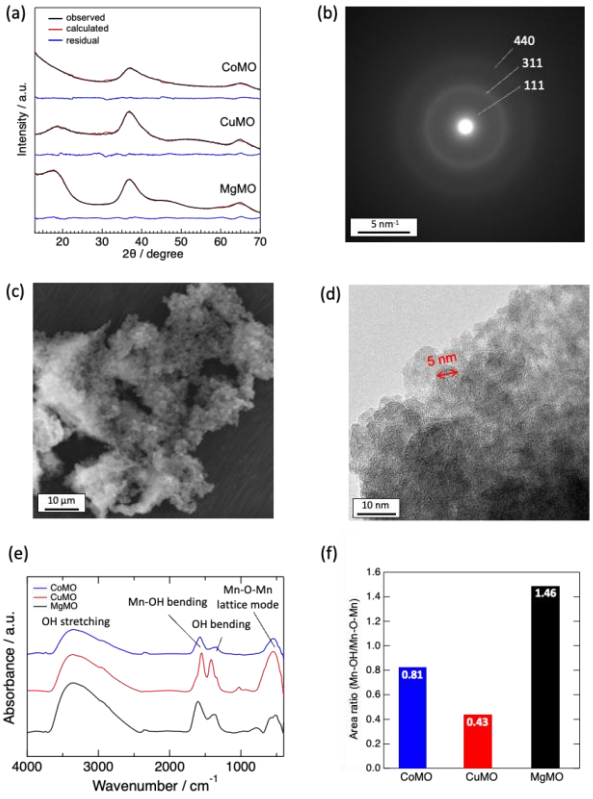

Figure 2. (a) XRD patterns with fitting curve by Rietveld refinement. (b) SAED pattern of CuMO. (c) SEM image of freeze-dried CuMO. (d) HR-TEM image of CuMO. (e) FT-IR spectra. (f) Summary of FT-IR peak area ratio (Mn-OH/Mn-O-Mn).

Figure 3a shows the voltage curves of each type of spinel. In the charge/discharge test, the upper cut-off voltage is set to 3.5 V considering the oxidative stability of electrolyte.[30] During the discharge process, the CoMO and MgMO cathodes display a capacity of approximately 100 mAh g^{-1}, which is less than half the theoretical capacity. Importantly, the MgMO synthesized in this study demonstrates a different discharge capacity than that reported in previous research.[24] This discrepancy could potentially be ascribed to variations in the primary particle size: approximately 5 nm in this study versus 2.1 nm in the prior work.

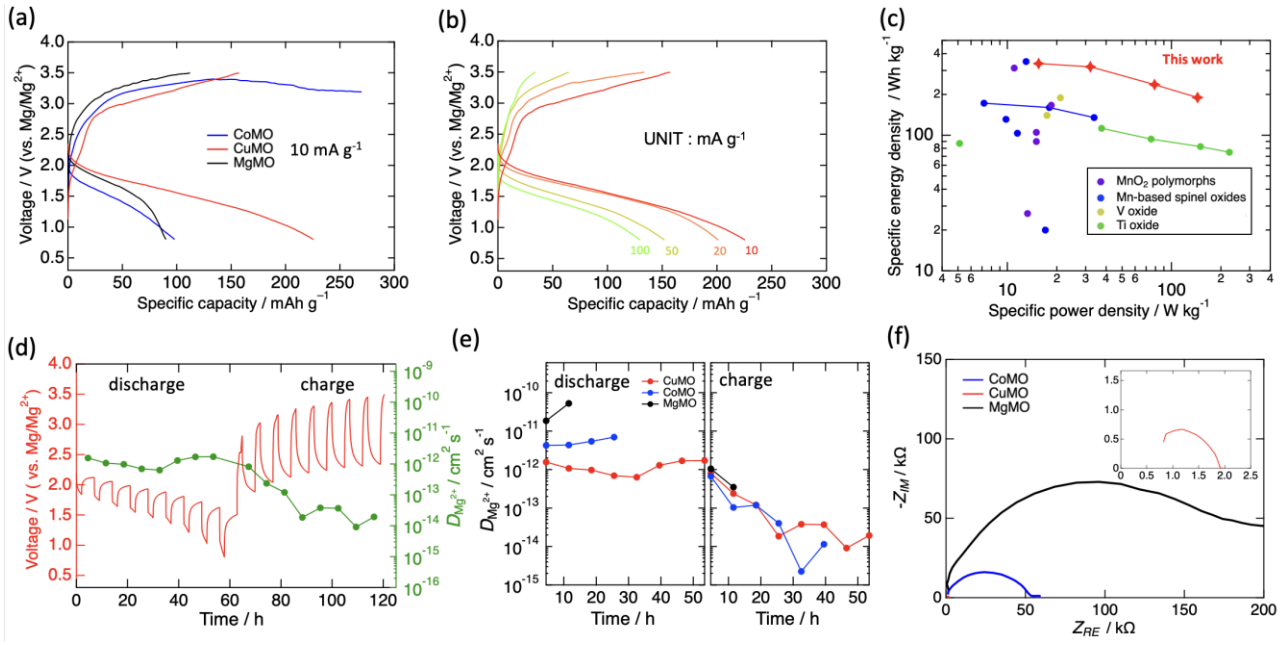

Figure 3. (a) Voltage curves of freeze-dried spinels. (b) Voltage curves with different rate capabilities of CuMO. (c) Ragone plot of the oxide-type cathodes. (d) GITT profiles and corresponding calculated Mg^{2+} diffusion coefficient of CuMO. (e) Calculated Mg^{2+} diffusion coefficient of each spinel. (f) Electrochemical impedance spectroscopy (EIS) spectra of each spinel.

These variations in size may have originated from the differences in the solvents used in the respective synthesis systems. In contrast, CuMO demonstrates a capacity of 225 mAh g^{-1}, exactly matching the theoretical expectation. Furthermore, CuMO exhibits the lowest overpotential during the charging process among the three types. However, only approximately 70% of the discharge capacity was recharged. This discrepancy can be attributed to the fact that the charged phase, specifically the rock-salt phase, is more stable than the spinel phase, which can hinder the extraction of Mg ions.[24] Regarding the cyclability shown in Figure S3, the discharge capacity decreases over the cycles, eventually stabilizing at approximately 70 mAh g^{-1}. In contrast, CoMO exhibits a plateau-like curve from 3.2 V. As stated in previous reports,[31-32] cobalt and manganese-containing spinels tend to have a higher valence band maximum than other spinels, which causes a continuous electron-withdrawal reaction through the cathode from the electrolyte. This suggests that the spinel oxides, which have high oxidative catalytic activity, can reduce the oxidative decomposition potential of the electrolyte. In addition, the DFT calculation revealed that the decomposition potential of the electrolyte is originated from the solvent. Taking monoglyme as an example, during the charging process, monoglyme in contact with spinel oxides undergoes fragmentation, transitioning from monoglyme to CH_3 + $CH_3OCH_2OCH_2$.[33] Figure 3b illustrates the voltage curves of CuMO at varying rates. Even though operation voltage was decreased as operation rate increased, CuMO exhibits specific discharge capacities of 225, 200, 153, and 130 mAh g^{-1} at 10, 20, 50, and 100 mA g^{-1}, respectively. These capacities are still superior to those of MgMO and CoMO at 10 mA g^{-1}, signifying that CuMO can sustain high-rate operations effectively. However, due to the difficulty of Mg ions extraction at charge state, as current density is increased, charge capacity decreases significantly. The Ragone plot, as presented in Figure 3c, provides a comparative assessment with oxide-type cathodes operating at room temperature. The developed ultra-small Cu-Mn spinel demonstrated high energy density coupled with high power density. This positions it as one of the highest-performing cathodes, setting it apart from other cathode materials.[17, 19, 24, 34-41]

To investigate the charge/discharge behavior, Galvanostatic Intermittent Titration Technique (GITT) measurements were performed, and the Mg^{2+} diffusion coefficient was calculated, as shown in Figure 3d and 3e. During the discharge process of CuMO, the IR drop value, which represents the overpotential inclusive of both the anode and cathode, progressively increases. Given the constant Mg dissolution resistance of the anode, the cathodic resistance increases as the voltage decreases. Based on a prior report,[42] this behavior can be attributed to the formation of a cathode electrolyte interphase (CEI) resulting from electrolyte reductive decompositions. Furthermore, SEM-EDX analysis of the electrode indirectly implies a side reaction. While the theoretical ratio of Mg insertion to Cu is 1.0, the observed ratio is 0.71, suggesting that the capacity, apart from Mg insertion, may originate from side reactions. Furthermore, MgMO and CoMO have higher Mg^{2+} diffusion coefficients than CuMO. The small Mg^{2+} diffusion coefficient of CuMO stems from the discrepancy of the crystalline phase. As shown in Figure 2b and Figure S1, CuMO has a smaller number of diffraction rings of SAED, indicating that the crystallinity of CuMO is lower than other spinels. This low crystallinity could be one of the factors to have higher diffusion barrier of Mg ions than those of other spinels. This result suggests that the superior discharge capacity of CuMO is not related to the Mg^{2+} diffusion coefficient. During the charging process, all spinels demonstrate considerably lower Mg^{2+} diffusion coefficients compared to those in the discharge process, as indicated by the large IR drop value for CuMO shown in Figure 3d. Although this can arise from a crystallographically stable phase, *i.e.*, the rock-salt phase, the diffusion coefficient values, ranging from 10^{-12} to 10^{-14} cm^2 S^{-1}, are substantially lower than the previously calculated value of 10^{-40} cm^2 S^{-1} for $Mg_2Mn_2O_4$.[24] This discrepancy may be due to the nanoparticulation of the cathode material, which is characterized by a metastable and low-crystallinity structure. This structure enhanced the Mg-ion kinetics during the charging process.

The electrical conductivity of each spinel was investigated using EIS measurements (Figure 3f). Out of the three, CuMO exhibited the lowest bulk resistance, and its electrical conductivity was found to be approximately 130 times greater than that

of MgMO. This observed trend is largely in agreement with a previous report,[38] considering that these cathode materials are porous and exhibit high grain boundary resistance. Thus far, our research has revealed that while CuMO has low Mg-ion conductivity, it possesses 100 times higher electrical conductivity than other spinels, which is a crucial factor influencing its high discharge capacity. Then, CuMO exhibits the high voltage operation (>1.5 V) with the theoretical discharge capacity of 225 mAh g^{-1}. To effectively operate an MRB at room temperature, the electrical conductivity of the cathode material is one of the most crucial considerations.

To confirm the redox species and their behavior in CuMO, we performed an X-ray absorption near-edge structure (XANES) analysis, as shown in Figure 4a. At the pristine state, the Mn *K*-edge position of CuMO overlaps with that of Mn_2O_3, indicating Mn^{3+}; as for Cu *K*-edge, a pre-edge peak around 8981 eV, a notable peak in Cu_2O, is not observed, suggesting Cu^{2+}. During discharge, the Mn *K*-edge spectrum shifted to a lower-energy region, indicating a reduction in Mn. Concurrently, the Cu *K*-edge spectrum also showed signs of reduction, as evidenced by the emergence of a pre-edge peak at approximately 8980 eV, which is characteristic of Cu^{+}. With respect to the charging process, although both the Mn *K*-edge and Cu *K*-edge spectra did not completely revert to their pristine states, we observed a partial reoxidation of Mn and Cu. This dual-redox system distinguishes CuMO from MgMO and CoMO. Specifically, by examining the CoMO redox, as indicated in Figures S4c and S4d, the Co *K*-edge spectra, and its derivative plots, we found that Co has little involvement in the redox processes. In addition, both CuMO and CoMO displayed partial reoxidation capabilities, whereas MgMO did not exhibit this characteristic. This observation can be attributed to the oxidative decomposition of the electrolyte, which was confirmed by XPS analysis.[43]

The dQ/dV plot of CuMO during discharge features two broad peaks around 1.7 V and 1.3 V. The former peak is also observed in MgMO, suggesting the reduction of Mn. On the other hand, the latter peak is unique in CuMO, indicating the reduction of Cu. Similarly, a peak at around 3.0 V in CuMO during charge can be attributed to the Cu oxidation. The Cu redox reaction of CuMO occurring on the lower-potential side has also been reported in a zinc-ion battery system.[44]

To trace changes in the crystalline phase, we performed electrode XRD measurements and SEM-EDX analysis, as shown in Figure 4b. During discharge, a peak emerged at approximately 34°, indicative of a rock-salt phase, whereas the 36° peak, signifying a spinel phase, diminished. In addition, in the charged state, an inverse reaction was observed between these peaks. This indicates that the spinel–rock-salt transition can occur not only in a high-temperature test,[14] but at room temperature. Owing to these changes in the crystalline phase, Mg insertion and extraction occurred. Specifically, in the charged state, approximately 0.29 of Mg was ejected, accounting for 82% of the theoretical charge capacity. This Mg extraction ability is markedly superior to those of MgMO and CuMO, which are known to struggle with electrolyte decomposition problems, as previously discussed.

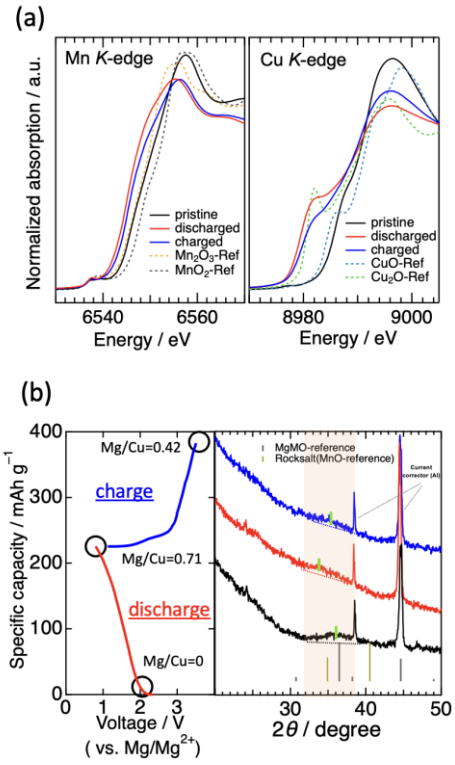

Figure 4. (a) Mn and Cu *K*-edge spectra of CuMO. (b) XRD patterns of CuMO electrode.

CONCLUSION

In this study, we developed an ultrasmall Cu-Mn spinel using an alcohol reduction process. This cathode material exhibits an exceptionally high voltage (>1.5 V) and a high capacity (225 mAh g^{-1}; theoretical capacity), distinguishing its performance from those of ultrasmall spinels. This superior cathodic performance stems from its high electrical conductivity, a crucial factor in cathode design. Moreover, our detailed analysis revealed that the ultrasmall Cu-Mn spinel is semi-reversible in terms of electrochemical phase transition and Mg insertion/extraction capability, which cannot be achieved by other spinels. With refinements in the material composition and the development of an electrolyte that can facilitate a broader electrochemical window, our synthesis strategy, which emphasizes both electrical conductivity and nanoparticulation, can establish a new standard for cathode materials in magnesium rechargeable batteries.

EXPERIMENTAL SECTION

Material synthesis. Ultrasmall A-Mn Oxides (A = Mg, Co, or Cu), denoted as MgMO, CoMO, and CuMO respectively, were synthesized using a modified alcohol reduction process (Figure 1). Initially, *n*-Bu_4NMnO_4, a Mn precursor, was synthesized by following a previously reported procedure.[26] In this process, a *n*-Bu_4NBr deionized water solution was slowly added dropwise into a $KMnO_4$ deionized water solution under vigorous stirring for an hour. The resulting precipitate: *n*-Bu_4NMnO_4 was washed with deionized water multiple times and dried under a vacuum overnight. As for the synthesis of MgMO and CoMO, the obtained *n*-Bu_4NMnO_4 (2 mmol) was added to a mixture of dehydrated $MgCl_2$ or $CoCl_2$ solution with methanol and ethylene glycol dimethyl ether solution (0.04 M, 50 mL, 1 to 1 volume ratio) under vigorous stirring for one hour. Regarding synthesis of CuMO, *n*-Bu_4NMnO_4 (2 mmol) was added to a methanol solution containing $Cu(CH_3COO)_2{\bullet}H_2O$ (0.02 M, 50 mL) under vigorous stirring for one hour. Subsequently, 10 mL

of deionized water was slowly added to each of the three brown colloidal solutions. The precipitate was washed with ethanol five times and heat-dried at 343 K under a vacuum overnight or freeze-dried from tert-butyl alcohol dispersion.

Material characterization. Powder X-ray diffraction (XRD) measurements were conducted using a Burker D2 PHASER 2ndGen instrument and SmartLab 3G insturument with Cu Kα radiation. The Rietveld refinement was performed using the RIETAN-FP program.[27] X-ray absorption spectroscopy (XAS) measurements were performed via the transmission method at the BL5S1 beamline of the Aichi Synchrotron Radiation Center. To ensure sample integrity, the samples were enclosed in an Al-laminated packaging film and affixed to a sample holder using Mn foil. The X-ray absorption near edge structure (XANES) analysis was carried out using the Athena program.[45] Transmission electron microscopy (TEM) images and scanning electron microscopy (SEM) were obtained using EM-002B and JSM-6010LA respectively. Elemental analysis was performed using inductively coupled plasma atomic emission spectroscopy (ICP-AES) on an Optima 3300XL (PerkinElmer) and SEM-EDX. Fourier Transform Infrared (FT-IR) spectra were obtained using Brunauer–Emmett–Teller (BET) surface areas of the sample were measured by N_2 adsorption at 77 K (BELSORP MAX G).

Electrochemical Measurements. The active material (MgMO, CoMO, or CuMO; 140 mg) was thoroughly mixed with acetylene black (AB; 40 mg) using a mortar for 10 minutes. Subsequently, the resulting mixture was added to a solution of N-methyl-pyrrolidone (NMP; 400 μL) containing polyvinylidenedifluoride (PVDF; 20 mg) and blended for 30 minutes. The resulting slurry, consisting of the active material, AB, and PVDF in a weight ratio of 70/20/10, was then pasted onto an Al foil and dried at 353 K for 2 hours. The dried electrode was shaped into a 7 mm-diameter disk with a mass loading of approximately 1.9 mg cm^{-2}. This prepared electrode was further dried at 343 K under vacuum for 12 hours and transferred to an Ar-filled glove box. For the anode material, Mg ribbon was cut to a length of 1 cm and polished using a metal file to remove any Mg oxide films. The cathode, anode, and electrolyte (0.3 M $Mg[B(HFIP)_4]_2$ / triglyme: G3, 150 μL) were assembled in a 2032-type coin cell with two glass-fiber separators (15 cm diameter, GA-55). Charge-discharge tests were conducted at 25 °C using a battery test system (HJ-1001SD8, Hokuto Denko Corp.) in constant-current (CC) mode.

GITT (galvanostatic intermittent titration technique) measurements were performed by alternating between a two-hour constant current impression and a five-hour rest period. The diffusion coefficient of Mg^{2+} was determined using the following equation:

$$\boldsymbol{D}_{\mathbf{Mg^{2+}}} = \frac{4}{\pi\tau}\left(\frac{n_M V_M}{S}\right)^2\left(\frac{\Delta E_S}{\Delta E_t}\right)^2 \quad \left(\tau \ll \frac{L^2}{D_{Mg^{2+}}}\right) \quad (1)$$

τ, n_M, V_M, and S represent rest time, molar quantity, molar volume, and electrode area respectively. ΔE_s and ΔE_t are the voltage differences. Note that L stands for the thickness of the electrode.

Electrochemical impedance spectroscopy (EIS) to measure bulk resistance was performed in a frequency range from 1 MHz to 0.1 Hz. 60 mg of sample powder was pressed at 200 MPa for 2 min using 10 mm-diameter dice to form a pellet. The obtained pellet was sandwiched with a 15 mm-diameter SUS316L disk and assembled in a 2032-type coin cell. Then, the bulk resistance was measured. Note that each sample was calcined at 573 K before the measurements in order to reduce grain boundary resistance by removing the surface OH group.

ASSOCIATED CONTENT

Supporting Information

The Supporting Information is available free of charge on the ACS Publications website.

SAED, SEM-EDX, HR-TEM, XANES, cycling performances (PDF)

AUTHOR INFORMATION

Corresponding Authors

Hiroaki Kobayashi – Department of Chemistry, Faculty of Science, Hokkaido University, Sapporo 060-0810, Japan; orcid.org/0000-0001-6705-9515; E-mail: h.kobayashi@sci.hokudai.ac.jp

Author Contributions

R.I.: Investigations and writing manuscript -draft-. H.W. and H.I.: Conceptualization. T.M.: Preparation of the electrolyte. I.H.: Supervision. H.K.: Conceptualization, methodology, project administration, funding acquisition. All co-authors contributed to writing manuscript - review & editing.

Notes

There are no conflicts to declare.

ACKNOWLEDGMENT

This work was supported by JST ALCA-SPRING (JPMJAL1301) and GteX (JPMJGX23S1), JSPS KAKENHI (23K1381603), Cooperative Research Program of NJRC Mater. & Dev. (MEXT), and the Light Metal Educational Foundation Japan.

REFERENCES

(1) Tarascon, J. M.; Armand, M. Issues and challenges facing rechargeable lithium batteries. *Nature* **2001,** *414*, 359-367, DOI: 10.1038/35104644.

(2) Yoo, H. D.; Shterenberg, I.; Gofer, Y.; Gershinsky, G.; Pour, N.; Aurbach, D. Mg rechargeable batteries: an on-going challenge. *Energy Env. Sci.* **2013,** *6*, 2265-2279, DOI: 10.1039/C3EE40871J.

(3) Bucur, C. B.; Gregory, T.; Oliver, A. G.; Muldoon, J. Confession of a Magnesium Battery. *J. Phys. Chem. Lett.* **2015,** *6*, 3578-3591, DOI: 10.1021/acs.jpclett.5b01219.

(4) Muldoon, J.; Bucur, C. B.; Gregory, T. Fervent Hype behind Magnesium Batteries: An Open Call to Synthetic Chemists—Electrolytes and Cathodes Needed. *Angew. Chem. Int. Ed.* **2017,** *56*, 12064-12084, DOI: 10.1002/anie.201700673.

(5) Li, Z.; Häcker, J.; Fichtner, M.; Zhao-Karger, Z. Cathode Materials and Chemistries for Magnesium Batteries: Challenges and Opportunities. *Adv. Energy Mater.* **2023,** *13* , 2300682, DOI: 10.1002/aenm.202300682.

(6) Aurbach, D.; Lu, Z.; Schechter, A.; Gofer, Y.; Gizbar, H.; Turgeman, R.; Cohen, Y.; Moshkovich, M.; Levi, E. Prototype systems for rechargeable magnesium batteries. *Nature* **2000,** *407*, 724-727, DOI: 10.1038/35037553.

(7) Mao, M.; Gao, T.; Hou, S.; Wang, F.; Chen, J.; Wei, Z.; Fan, X.; Ji, X.; Ma, J.; Wang, C. High-Energy-Density Rechargeable Mg Battery Enabled by a Displacement Reaction. *Nano Lett.* **2019,** *19*, 6665-6672, DOI: 10.1021/acs.nanolett.9b02963.

(8) Fei, Y.; Man, Y.; Sun, J.; Du, Y.; Chen, B.; Bao, J.; Zhou, X. Implanting CuS Quantum Dots into Carbon Nanorods for Efficient Magnesium-Ion Batteries. *Small* **2023,** *19* , 2301954, DOI: 10.1002/smll.202301954.

(9) Xue, X.; Song, X.; Tao, A.; Yan, W.; Zhang, X. L.; Tie, Z.; Jin, Z. Boosting the cycling stability of rechargeable magnesium batteries by regulating the compatibility between nanostructural metal sulfide cathodes and non-nucleophilic electrolytes. *Nano Res.* **2023,** *16*, 2399-2408, DOI: 10.1007/s12274-022-4932-z.

(10) Li, Z.; Vinayan, B. P.; Jankowski, P.; Njel, C.; Roy, A.; Vegge, T.; Maibach, J.; Lastra, J. M. G.; Fichtner, M.; Zhao-Karger, Z. Multi-Electron Reactions Enabled by Anion-Based Redox Chemistry for High-Energy Multivalent Rechargeable Batteries. *Angew. Chem. Int. Ed.* **2020,** *59*, 11483-11490, DOI: 10.1002/anie.202002560.

(11) Jankowski, P.; Lastra, J. M. G. Towards the understanding of (dis)charging mechanism of VS_4 cathode for magnesium batteries. *J. Energy Stor.* **2023,** *62*, 106895, DOI: 10.1016/j.est.2023.106895.
(12) Rashad, M.; Asif, M.; Ahmed, I.; He, Z.; Yin, L.; Wei, Z. X.; Wang, Y. Quest for carbon and vanadium oxide based rechargeable magnesium-ion batteries. *J. Magnesium Alloys* **2020,** *8*, 364-373, DOI: 10.1016/j.jma.2019.09.010.
(13) Johnson, I. D.; Ingram, B. J.; Cabana, J. The Quest for Functional Oxide Cathodes for Magnesium Batteries: A Critical Perspective. *ACS Energy Lett.* **2021,** *6*, 1892-1900, DOI: 10.1021/acsenergylett.1c00416.
(14) Okamoto, S.; Ichitsubo, T.; Kawaguchi, T.; Kumagai, Y.; Oba, F.; Yagi, S.; Shimokawa, K.; Goto, N.; Doi, T.; Matsubara, E. Intercalation and Push-Out Process with Spinel-to-Rocksalt Transition on Mg Insertion into Spinel Oxides in Magnesium Batteries. *Adv. Sci.* **2015,** *2*, 1500072, DOI: 10.1002/advs.201500072.
(15) Truong, Q. D.; Kempaiah Devaraju, M.; Tran, P. D.; Gambe, Y.; Nayuki, K.; Sasaki, Y.; Honma, I. Unravelling the Surface Structure of $MgMn_2O_4$ Cathode Materials for Rechargeable Magnesium-Ion Battery. *Chem. Mater.* **2017,** *29*, 6245-6251, DOI: 10.1021/acs.chemmater.7b01252.
(16) Shimokawa, K.; Atsumi, T.; Okamoto, N. L.; Kawaguchi, T.; Imashuku, S.; Wagatsuma, K.; Nakayama, M.; Kanamura, K.; Ichitsubo, T. Structure Design of Long-Life Spinel-Oxide Cathode Materials for Magnesium Rechargeable Batteries. *Adv. Mater.* **2021,** *33*, 2007539, DOI: 10.1002/adma.202007539.
(17) Yoo, H. D.; Jokisaari, J. R.; Yu, Y.-S.; Kwon, B. J.; Hu, L.; Kim, S.; Han, S.-D.; Lopez, M.; Lapidus, S. H.; Nolis, G. M.; Ingram, B. J.; Bolotin, I.; Ahmed, S.; Klie, R. F.; Vaughey, J. T.; Fister, T. T.; Cabana, J. Intercalation of Magnesium into a Layered Vanadium Oxide with High Capacity. *ACS Energy Lett.* **2019,** *4*, 1528-1534, DOI: 10.1021/acsenergylett.9b00788.
(18) Arthur, T. S.; Zhang, R.; Ling, C.; Glans, P.-A.; Fan, X.; Guo, J.; Mizuno, F. Understanding the Electrochemical Mechanism of K-αMnO_2 for Magnesium Battery Cathodes. *ACS Appl. Mater. Interfaces* **2014,** *6*, 7004-7008, DOI: 10.1021/am5015327.
(19) Kwon, B. J.; Yin, L.; Park, H.; Parajuli, P.; Kumar, K.; Kim, S.; Yang, M.; Murphy, M.; Zapol, P.; Liao, C.; Fister, T. T.; Klie, R. F.; Cabana, J.; Vaughey, J. T.; Lapidus, S. H.; Key, B. High Voltage Mg-Ion Battery Cathode via a Solid Solution Cr–Mn Spinel Oxide. *Chem. Mater.* **2020,** *32*, 6577-6587, DOI: 10.1021/acs.chemmater.0c01988.
(20) Yin, L.; Kwon, B. J.; Choi, Y.; Bartel, C. J.; Yang, M.; Liao, C.; Key, B.; Ceder, G.; Lapidus, S. H. Operando X-ray Diffraction Studies of the Mg-Ion Migration Mechanisms in Spinel Cathodes for Rechargeable Mg-Ion Batteries. *J. Am. Chem. Soc.* **2021,** *143*, 10649-10658, DOI: 10.1021/jacs.1c04098.
(21) Kobayashi, H.; Yamaguchi, K.; Honma, I. Rapid room-temperature synthesis of ultrasmall cubic Mg–Mn spinel cathode materials for rechargeable Mg-ion batteries. *RSC Adv.* **2019,** *9*, 36434-36439, DOI: 10.1039/C9RA08626A.
(22) Yokozaki, R.; Kobayashi, H.; Honma, I. Reductive solvothermal synthesis of $MgMn_2O_4$ spinel nanoparticles for Mg-ion battery cathodes. *Ceram. Int.* **2021,** *47* , 10236-10241, DOI: 10.1016/j.ceramint.2020.10.184.
(23) Kobayashi, H.; Samukawa, K.; Nakayama, M.; Mandai, T.; Honma, I. Promoting Reversible Cathode Reactions in Magnesium Rechargeable Batteries Using Metastable Cubic $MgMn_2O_4$ Spinel Nanoparticles. *ACS Appl. Nano Mater.* **2021,** *4*, 8328-8333, DOI: 10.1021/acsanm.1c01519.
(24) Kobayashi, H.; Fukumi, Y.; Watanabe, H.; Iimura, R.; Nishimura, N.; Mandai, T.; Tominaga, Y.; Nakayama, M.; Ichitsubo, T.; Honma, I.; Imai, H. Ultraporous, Ultrasmall $MgMn_2O_4$ Spinel Cathode for a Room-Temperature Magnesium Rechargeable Battery. *ACS Nano* **2023,** *17*, 3135-3142, DOI: 10.1021/acsnano.2c12392.
(25) Johnson, I. D.; Mistry, A. N.; Yin, L.; Murphy, M.; Wolfman, M.; Fister, T. T.; Lapidus, S. H.; Cabana, J.; Srinivasan, V.; Ingram, B. J. Unconventional Charge Transport in $MgCr_2O_4$ and Implications for Battery Intercalation Hosts. *J. Am. Chem. Soc.* **2022,** *144*, 14121-14131, DOI: 10.1021/jacs.2c03491.
(26) Sugawara, Y.; Kobayashi, H.; Honma, I.; Yamaguchi, T. Effect of Metal Coordination Fashion on Oxygen Electrocatalysis of Cobalt–Manganese Oxides. *ACS Omega* **2020,** *5*, 29388-29397, DOI: 10.1021/acsomega.0c04254.
(27) Izumi, F.; Momma, K. Three-Dimensional Visualization in Powder Diffraction. *Solid State Phenom.* **2007,** *130*, 15-20, DOI: 10.4028/www.scientific.net/SSP.130.15.
(28) Ramadan, W.; AlSalka, Y.; Al-Madanat, O.; Bahnemann, D. W. Synthesis of Magnetic Ferrite and TiO_2-Based Nanomaterials for Photocatalytic Water Splitting Applications. In *Synthesis and Applications of Nanomaterials and Nanocomposites*; Uddin, I.; Ahmad, I., Eds.; Springer Nature Singapore: Singapore, 2023; pp 293-329.
(29) Pauling, L. THE NATURE OF THE CHEMICAL BOND. IV. THE ENERGY OF SINGLE BONDS AND THE RELATIVE ELECTRONEGATIVITY OF ATOMS. *J. Am. Chem. Soc.* **1932,** *54*, 3570-3582, DOI: 10.1021/ja01348a011.
(30) Zhao-Karger, Z.; Liu, R.; Dai, W.; Li, Z.; Diemant, T.; Vinayan, B. P.; Bonatto Minella, C.; Yu, X.; Manthiram, A.; Behm, R. J.; Ruben, M.; Fichtner, M. Toward Highly Reversible Magnesium–Sulfur Batteries with Efficient and Practical $Mg[B(hfip)_4]_2$ Electrolyte. *ACS Energy Lett.* **2018,** *3*, 2005-2013, DOI: 10.1021/acsenergylett.8b01061.
(31) Zhang, C.; Peng, Z.; Chen, Y.; Chen, H.; Zhang, B.; Cheng, H.; Wang, J.; Deng, M. Efficient coupling of semiconductors into metallic MnO_2@$CoMn_2O_4$ heterostructured electrode with boosted charge transfer for high-performance supercapacitors. *Electrochim. Acta* **2020,** *347*, 136246, DOI: 10.1016/j.electacta.2020.136246.
(32) Han, J.; Yagi, S.; Takeuchi, H.; Nakayama, M.; Ichitsubo, T. Catalytic mechanism of spinel oxides for oxidative electrolyte decomposition in Mg rechargeable batteries. *J. Mater. Chem. A* **2021,** *9*, 26401-26409, DOI: 10.1039/D1TA08115B.
(33) Zhou, W.; Xu, C.; Gao, B.; Nakayama, M.; Yagi, S.; Tateyama, Y. Glyme Solvent Decomposition on Spinel Cathode Surface in Magnesium Battery. *ACS Energy Lett.* **2023,** *8*, 4113-4118, DOI: 10.1021/acsenergylett.3c01084.
(34) Koketsu, T.; Ma, J.; Morgan, B. J.; Body, M.; Legein, C.; Dachraoui, W.; Giannini, M.; Demortière, A.; Salanne, M.; Dardoize, F.; Groult, H.; Borkiewicz, O. J.; Chapman, K. W.; Strasser, P.; Dambournet, D. Reversible magnesium and aluminium ions insertion in cation-deficient anatase TiO_2. *Nat. Mater.* **2017,** *16*, 1142-1148, DOI: 10.1038/nmat4976.
(35) Wang, Y.; Xue, X.; Liu, P.; Wang, C.; Yi, X.; Hu, Y.; Ma, L.; Zhu, G.; Chen, R.; Chen, T.; Ma, J.; Liu, J.; Jin, Z. Atomic Substitution Enabled Synthesis of Vacancy-Rich Two-Dimensional Black TiO_{2-x} Nanoflakes for High-Performance Rechargeable Magnesium Batteries. *ACS Nano* **2018,** *12*, 12492-12502, DOI: 10.1021/acsnano.8b06917.
(36) Rastgoo-Deylami, M.; Chae, M. S.; Hong, S.-T. $H_2V_3O_8$ as a High Energy Cathode Material for Nonaqueous Magnesium-Ion Batteries. *Chem. Mater.* **2018,** *30*, 7464-7472, DOI: 10.1021/acs.chemmater.8b01381.
(37) Fu, Q.; Sarapulova, A.; Trouillet, V.; Zhu, L.; Fauth, F.; Mangold, S.; Welter, E.; Indris, S.; Knapp, M.; Dsoke, S.; Bramnik, N.; Ehrenberg, H. In Operando Synchrotron Diffraction and in Operando X-ray Absorption Spectroscopy Investigations of Orthorhombic V_2O_5 Nanowires as Cathode Materials for Mg-Ion Batteries. *J. Am. Chem. Soc.* **2019,** *141*, 2305-2315, DOI: 10.1021/jacs.8b08998.
(38) Takemitsu, H.; Hayashi, Y.; Watanabe, H.; Mandai, T.; Yagi, S.; Oaki, Y.; Imai, H. Preparation of conductive $Cu_{1.5}Mn_{1.5}O_4$ and Mn_3O_4 spinel mixture powders as positive active materials in rechargeable Mg batteries operative at room temperature. *J. Sol-Gel Sci. Technol.* **2022,** *104*, 635-646, DOI: 10.1007/s10971-022-05891-0.
(39) Ye, X.; Li, H.; Hatakeyama, T.; Kobayashi, H.; Mandai, T.; Okamoto, N. L.; Ichitsubo, T. Examining Electrolyte Compatibility on Polymorphic MnO_2 Cathodes for Room-Temperature Rechargeable Magnesium Batteries. *ACS Appl. Mater. Interfaces* **2022,** *14*, 56685-56696, DOI: 10.1021/acsami.2c14193.
(40) Mandai, T.; Somekawa, H. Ultrathin Magnesium Metal Anode – An Essential Component for High-Energy-Density Magnesium Battery Materialization. *Batteries & Supercaps* **2022,** *5*, e202200153, DOI: 10.1002/batt.202200153.
(41) Idemoto, Y.; Takamatsu, M.; Ishibashi, C.; Ishida, N.; Mandai, T.; Kitamura, N. Electrochemical properties and crystal and electronic structure changes during charge/discharge of spinel type cathode-materials $Mg_{1.33}V_{1.67-x}Mn_xO_4$ for magnesium secondary batteries. *J. Electroanal. Chem.* **2023,** *928*, 117064, DOI: 10.1016/j.jelechem.2022.117064.
(42) Han, J.; Yagi, S.; Takeuchi, H.; Nakayama, M.; Ichitsubo, T. Control of Electrolyte Decomposition by Mixing Transition Metal Ions in Spinel Oxides as Positive Electrode Active Materials for Mg Rechargeable Batteries. *J. Phys. Chem. C* **2022,** *126*, 19074-19083, DOI: 10.1021/acs.jpcc.2c06443.
(43) Iimura, R.; Kobayashi, H.; Honma, I. Suppressing Electrolyte Decomposition at Cathode/Electrolyte Interface by Mg-Fe Binary Oxide Coating towards Room-Temperature Magnesium Rechargeable Battery Operation. *Electrochemistry* **2022,** *90*, 067002-067002, DOI: 10.5796/electrochemistry.22-00045.
(44) Yang, G.; Ma, K.; Wang, C. Unconventional Copper Electrochemistry in Aqueous Zn ‖ $CuMn_2O_4$ Batteries. *Adv. Energy Mater.* **2024,** *14*, 2303695, DOI: 10.1002/aenm.202303695.
(45) Ravel, B.; Newville, M. ATHENA, ARTEMIS, HEPHAESTUS: data analysis for X-ray absorption spectroscopy using IFEFFIT. *J. Synchrotron Rad.* **2005,** *12*, 537-541, DOI: 10.1107/S0909049505012719.

TOC graphic

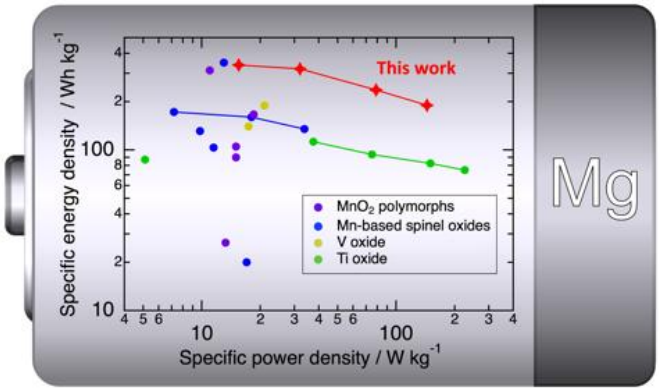
Specific energy density / Wh kg-1
Specific power density / W kg-1
This work
MnO2 polymorphs
Mn-based spinel oxides
V oxide
Ti oxide
Mg